An Interlayer Anchored NiMo/MoO$_2$ Electrocatalyst for Hydrogen Evolution Reaction in Anion Exchange Membrane Water Electrolysis at High Current Density

Gaoxin Lin, Anrui Dong, Zhiheng Li, Wenlong Li, Xing Cao, Yilong Zhao, Linqin Wang, and Licheng Sun*

Noble metal-free electrodes for anion exchange membrane water electrolysis (AEM-WE) operating at high current densities are critical for sustainable hydrogen production. However, the massive amount of bubbles resulted in insufficient mass transfer and unevenly distributed local stress, which poses a major challenge in designing an efficient and robust hydrogen evolution catalyst. Herein, a facile chemical corrosion method is developed to synthesize an interlayer-anchored NiMo/MoO$_2$ catalyst on a nickel foam (NF) substrate (NiMo/Int/NF) with high hydrogen evolution activity (overpotential of 80.2 $\pm$ 3.53 mV) and durability (stable for 5000 h) at 1000 mA cm^{-2} in 1 M KOH. The interlayer tightly anchors the catalytic layer to the substrate, providing high compressive strength and strong adhesion to mitigate the bubble shock at a high current density. In situ Raman and X-ray diffraction analyses reveal that the heterostructural catalytic layer can accelerate the hydrogen evolution reaction with increased local pH and high component utilization. Using NiMo/Int/NF as the cathode, the assembled noble metal-free AEM-WE device exhibits a low cell voltage of 1.78 V at 1000 mA cm^{-2} (significantly lower than that of a Pt/C-catalyzed cell (1.94 V)) while also showing excellent stability for 3000 h.

1. Introduction

Water electrolysis is a promising hydrogen generation technology, harnessing intermittent renewable energy sources such as solar, wind, and waves.[1] Anion exchange membrane water electrolysis (AEM-WE) plays a crucial role in sustainable hydrogen production, as it combines the advantages of alkaline water electrolysis (low cost and relative stability) and proton exchange membrane water electrolysis (high current density, fast startup, and high safety).[2] However, designing efficient and robust cathodic electrodes with non-noble metals for high-current-density AEM-WEs remains challenging.[3] The rate of the hydrogen evolution reaction (HER) at the cathode is twice that of the oxygen evolution reaction (OER) at the anode, resulting in severe charge transfer (electron exchange at the liquid-solid interface),[3a,4] mass transfer (ion diffusion and gas release at the gas–liquid-solid interface),[5] and mechanical instability (bubble shock within the catalytic layer).[4a,6]

Self-supported electrodes, including transition metal alloys, oxides, sulfides, phosphides, and compounds,[7] with catalytically active phases grown in situ on conductive substrates, have been widely studied in HERs. Among them, Ni-Mo-based electrodes show great potential for high-current-density HER.[8] The 3D and well-defined catalytic layer of a self-supported electrode provides abundant active sites and hierarchical channels, promoting the catalytic reaction and electrolyte diffusion during HER. However, most Ni-Mo-based electrodes are synthesized through the hydrothermal method at high temperatures ($\geq$120 °C), which limits their scalability for AEM-WE. Additionally, achieving high intrinsic activity with fast H—OH bond cleavage kinetics is essential for surface adsorption/desorption processes at high current densities.[9] Moreover, the constant impact of bubbles on the interface between the catalyst and substrate can cause mechanical stress, leading to catalyst fragmentation and detachment.[10] An interlayer between the substrate and catalyst has been introduced to reinforce their interactions for stable OER to mitigate this issue.[2c] Interlayer-anchored HER electrodes with high stability and scalability remain unsatisfactory. Therefore, developing an efficient HER catalyst that can operate at a high current density for a long time presents a major challenge in the industrialization of AEM-WEs.

G. Lin, A. Dong, Z. Li, W. Li, X. Cao, Y. Zhao, L. Wang, L. Sun
Center of Artificial Photosynthesis for Solar Fuels and Department of Chemistry
School of Science and Research Center for Industries of the Future
Westlake University
600 Dunyu Road, Hangzhou, Zhejiang 310030, China
E-mail: sunlicheng@westlake.edu.cn
G. Lin, A. Dong, Z. Li, W. Li, X. Cao, Y. Zhao, L. Wang, L. Sun
Institute of Natural Sciences
Westlake Institute for Advanced Study
18 Shilongshan Road, Hangzhou, Zhejiang 310024, China
L. Sun
Division of Solar Energy Conversion and Catalysis at Westlake University
Zhejiang Baima Lake Laboratory Co., Ltd.
Hangzhou, Zhejiang 310000, China

**ADVANCED
SCIENCE NEWS**

www.advancedsciencenews.com

**ADVANCED
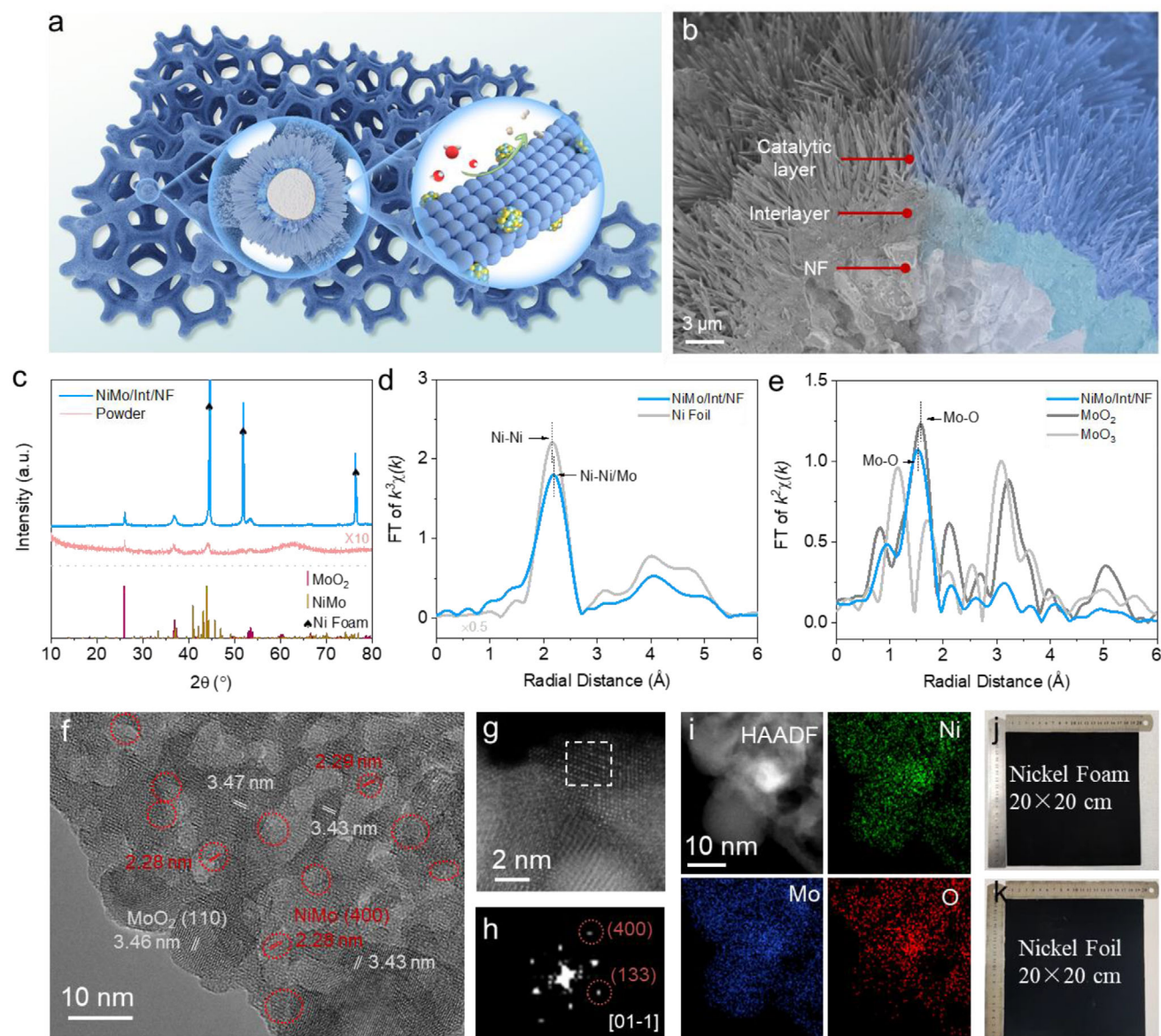MATERIALS**

www.advmat.de

Figure 1. Morphology and structure of NiMo/Int/NF. a) Schematic illustration of the NiMo/Int/NF catalyst with an interlayer-anchored NiMo/MoO$_2$ catalytic layer. b) Cross-sectional SEM image of NiMo/Int/NF, which consists of a rod-like catalytic layer anchored on the NF substrate by an interlayer. c) XRD patterns of NiMo/Int/NF on foam and its powder. d) Fourier transformed EXAFS spectra of NiMo/Int/NF and Ni foil at the Ni K-edge in R-space. e) Fourier transformed EXAFS spectra of NiMo/Int/NF, MoO$_2$, and MoO$_3$ at the Mo K-edge in R-space. f) HR-TEM image of NiMo/Int/NF. The red cycles correspond to the NiMo nanoparticles. g) HAADF-STEM image of NiMo/Int/NF. h) Fourier transform pattern from the site in g. i) EDX elemental mapping of NiMo/Int/NF. j) Photo of NiMo/Int/NF synthesized on NF. k) Photo of NiMo/Int/NF synthesized on nickel foil.

Herein, we report a facile and scalable corrosion method for synthesizing interlayer-anchored NiMo/MoO$_2$ heterostructures on nickel foam (NF) substrates (NiMo/Int/NF, **Figure 1a**). The heterostructural catalytic layer with high component utilization rates facilitates the cleavage of the H—OH bond in the Volmer step, resulting in a high local pH. The corrosion-induced interlayer bonds the catalytic layer tightly to the substrate, offering high mechanical stability and reducing the fluctuations at high current densities up to 6000 mA cm^{-2}. When combined with a nonprecious nickel iron-based anode catalyst, the AEM-WE device exhibits a high activity of 1.78 V at 1000 mA cm^{-2}

and long-term stability for 3000 h with a low degradation rate of 22.8 µV h^{-1} at room temperature.

2. Results and Discussion

NiMo/Int/NF was synthesized by soaking NF in a molybdate peroxide solution at 80 °C for 24 h to undergo chemical corrosion on the substrate and grow a nickel molybdate precursor. Scanning electron microscopy (SEM) images revealed the uniform growth of the rod-like and porous catalyst on the NF (Figure S1, Supporting Information). In addition, cross-sectional SEM

images indicate a dense interlayer, which serves as a glue to tightly anchor the catalytic layer on the NF (Figure 1b; Figure S1c, Supporting Information). Energy-dispersive X-ray spectroscopy (EDX) confirmed the same elemental composition of Ni, Mo, and O for the interlayer and catalytic layer (Figure S2, Supporting Information). X-ray diffraction (XRD) patterns indicated that the NiMo/Int/NF heterostructure contains an orthorhombic NiMo alloy and monoclinic MoO_2 (Figure 1c). The extended X-ray absorption fine structure (EXAFS) spectrum of the Ni K-edge shows a stronger Ni−Ni/Mo scattering path in NiMo/Int/NF compared to the Ni−Ni scattering path in Ni foil (Figure 1d), confirming the presence of NiMo alloy in NiMo/Int/NF (Figure S3 and Table S1, Supporting Information). The EXAFS spectrum of the Mo K-edge also confirms that the Mo−O shells of NiMo/Int/NF are similar to those of MoO_2 (Figure 1e). Moreover, the $NiMo/MoO_2$ heterostructure was verified using high-resolution transmission electron microscopy (HR-TEM), which revealed numerous MoO_2 and NiMo nanoparticles (Figure 1f). High-angle annular dark-field imaging-scanning transmission electron microscopy (HAADF-STEM) and Fourier transform patterns further confirmed the presence of the (400) and (133) lattice planes in the NiMo alloy (Figure 1g,h). EDX indicated that the NiMo nanoparticles were uniformly anchored on the MoO_2 substrate (Figure 1i). TEM images of focus ion beam thinned NiMo/Int/NF lamella confirmed the solid interaction between the catalyst structure and NF substrate, providing strong adhesion and efficient charge transfer at the interface (Figure S4, Supporting Information). Based on the ex situ SEM and X-ray photoelectron spectroscopy (XPS) results, chemical corrosion occurred during the initial 2 h, followed by the growth of the catalytic layer (Figures S5 and S6, Supporting Information). The grazing incidence X-ray diffraction (GIXRD) patterns revealed the same $NiMo/MoO_2$ structure of the interlayer and catalytic layer, but their crystallinity differs (Figure S7, Supporting Information). The photos in Figure 1j,k demonstrate that the soaking method could easily prepare a large-sized catalyst layer on NF (roughness factor of 27.57 ± 1.66) and even on nickel foil (roughness factor of 5.98 ± 0.02) with high uniformity and consistency (Figures S8–S10, Supporting Information).

The HER activity of NiMo/Int/NF was evaluated in an alkaline electrolyte using Hg/HgO as the reference electrode and a graphite plate as the counter electrode. For comparison, a NiMo/NF sample, which has the same heterostructure as NiMo/Int/NF but lacks the interlayer, was also synthesized using a soaking method (Figures S11 and S12, Supporting Information). The linear sweep voltammetry (LSV) curves show a low overpotential of 28.1 ± 2.0 mV for NiMo/Int/NF at 100 mA cm^{-2}, which is lower than those for NiMo/NF (35.7 ± 1.4 mV) and Pt/C (61.4 ± 2.5 mV) (**Figure 2a**). Moreover, the overpotentials of NiMo/Int/NF increased slightly to 80.2 ± 3.53 and 121.5 ± 6.2 mV at high current densities of 1000 and 2000 mA cm^{-2}, respectively (Figure S13, Supporting Information). Compared to NiMo/NF, the higher activity of NiMo/Int/NF was due to its low charge transfer resistance during catalysis and high mass loading (Figures S12 and S14 and Table S2, Supporting Information). The Tafel slopes derived from steady-state potentials are 60.1 and 55.2 mV dec^{-1} for NiMo/Int/NF and Pt/C, respectively, at low current densities (≤ 22 mV cm^{-2}, Figure S15, Supporting Information). These values fall between 40 mV (rate-determining step

(RDS) of the Heyrovsky step) and 120 mV (RDS of the Volmer step),[11] suggesting that the reactions are influenced by hydrogen rearrangement.[12] To explore the mechanism underlying the high activity of NiMo/Int/NF, in situ Raman measurements were conducted in a mixed solution of $KHCO_3$ and K_2CO_3 to determine the local pH during catalysis (Figure 2b,c; Figure S16, Supporting Information). When a Pt/C electrode was used, the concentration of HCO_3^- increased after a potential was applied (Figure 2d), indicating a decrease in the local pH.[13] However, the local pH of NiMo/Int/NF increased during the HER, suggesting that the electrode surface exhibited a significantly different hydrogen concentration.[14] In addition, a rotating ring-disk electrode (RRDE) was used to evaluate the local pH of the diffuse layer adjacent to the bulk during catalysis.[15] In a 1 M phosphate buffer solution (PBS, pH 7), the local pH of Pt/C remained constant at ≈7 before and after HER (Figure 2e; Figure S17, Supporting Information). However, the initial pH of NiMo/Int/NF was slightly higher than that of the electrolyte and further increased after HER; thus, the heterostructure of NiMo and MoO_2 could promote the cleavage of H−OH and the formation of H_2 on the surface, resulting in a higher local pH.

Electrochemical impedance spectroscopy (EIS) reveals peaks at 1–5 Hz in the Bode plot of NiMo/Int/NF and NiMo/NF (Figure S18a,b, Supporting Information). The low-frequency signal is associated with the Volmer step.[16] The peak at the middle frequency of 10–50 Hz for Pt/C corresponds to the Heyrovsky step (Figure S18c, Supporting Information). Based on kinetic isotope effect (KIE) measurements, NiMo/Int/NF exhibited a higher KIE value than Pt/C (Figure S19, Supporting Information), confirming a higher degree of proton involvement. Moreover, in situ XRD measurements show that the full width at half maximum increases from an open circuit potential (OCP) to −0.10 V (Figure S20, Supporting Information). This indicates a decrease in the crystallinity of MoO_2 (110). The crystallinity recovered when the potential returned to the OCP (Figure 2f). This crystallinity change demonstrates the adsorption of intermediates on the surface of NiMo/Int/NF, implying the high utilization rate of the components during the catalytic process. Based on the above results, the high electrochemical activity of NiMo/Int/NF can be attributed to the synergistic effect within the heterostructure of NiMo and MoO_2,[3c,17] in which the formation of adsorbed hydrogen (Volmer step) is the RDS (Figure 2g). A faster Heyrovsky step reduces the hydrogen concentration on the catalyst surface, resulting in an increased local pH, as shown by the in situ Raman measurements.[18] For the Pt/C electrode, the slow Heyrovsky step cannot consume the protons formed in the fast Volmer step, leading to an acidic microenvironment during catalysis.[14]

The role of the interlayer in NiMo/Int/NF was investigated by mechanical performance testing. Nanoindentation measurements indicate a lower maximum indentation depth (h_{max}, 636.9 ± 37.1 nm) and a lower final depth (h_f, 503.0 ± 38.3 nm) for NiMo/Int/NF (**Figure 3a**) compared to NiMo/NF without an interlayer (h_{max} of 2163.9 ± 67.5 nm, h_f of 1836.9 ± 101.2 nm). Thus, the high compressive strength of NiMo/Int/NF can prevent catalyst shattering under intense bubble shock during HER.[10a,19] In addition, nanoscratch measurements confirm a strong adhesion force between the catalytic layer and the substrate for NiMo/Int/NF (Figure 3b), enabling it to endure the bubble-induced uneven stress distribution and prevent catalyst
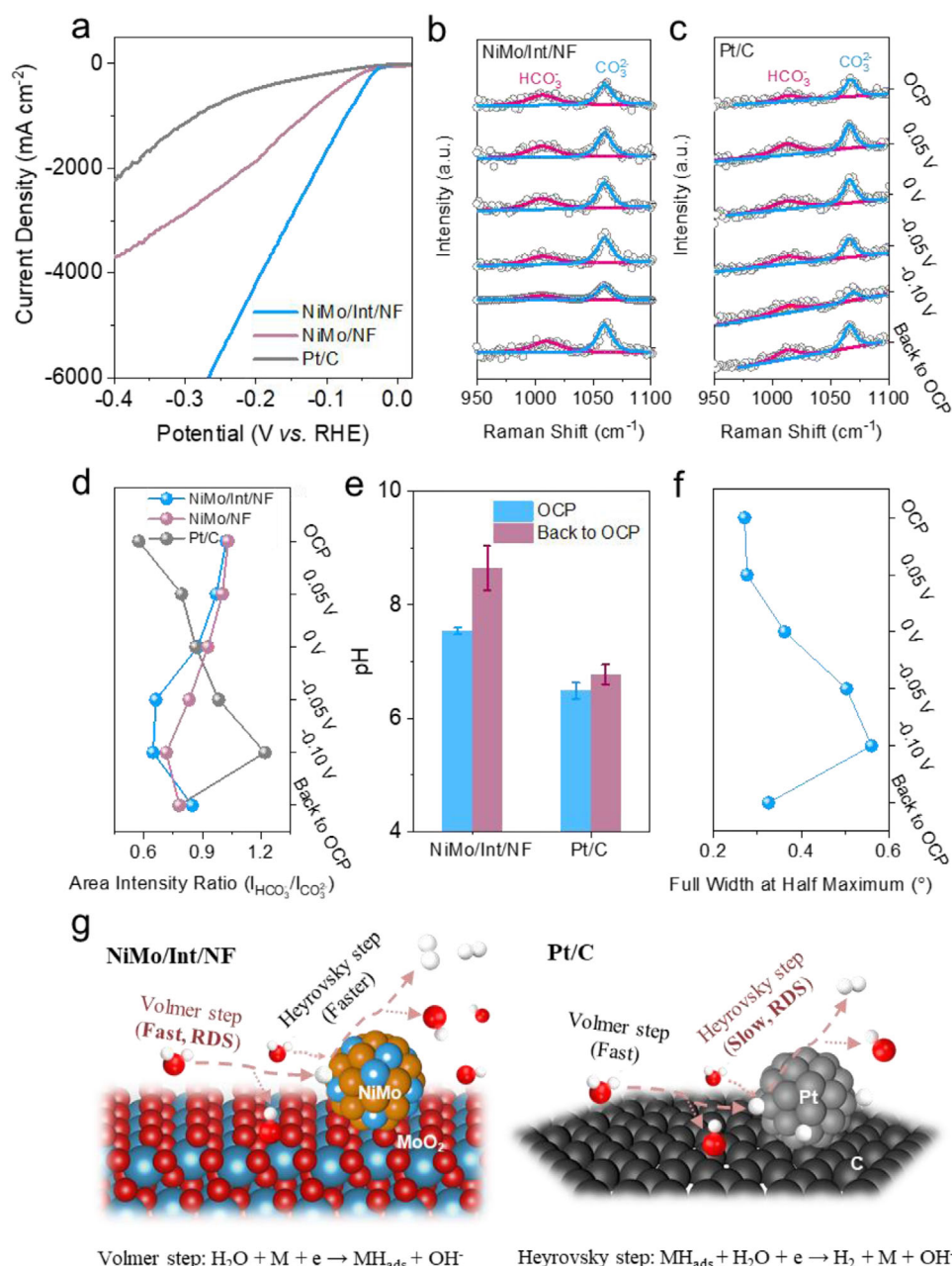
**ADVANCED
SCIENCE NEWS**

www.advancedsciencenews.com

**ADVANCED
MATERIALS**

www.advmat.de

Figure 2. HER mechanisms. a) Polarization curves of NiMo/Int/NF, NiMo/NF, and Pt/C in 1 M KOH. b) In situ Raman spectra of NiMo/Int/NF in a mixed solution of $KHCO_3$ and K_2CO_3. c) In situ Raman spectra of Pt/C. d) Area-intensity ratio of HCO_3^- and CO_3^{2-} obtained from in situ Raman spectra. e) Local pH derived from RRDE measurements for NiMo/Int/NF and Pt/C in 1 M PBS (pH 7). f) Full width at half maximum of MoO_2 (110) obtained from in situ XRD. g) Schematic of HER mechanisms for NiMo/Int/NF and Pt/C.

peeling.[5b,20] Multiple current tests (in the range of 1000 to 6000 mA cm^{-2}) were carried out to evaluate the mechanical stability during catalysis. As shown in Figure 3c, when the current density increased, potential fluctuations in the NiMo/NF electrode became more pronounced due to the pressure shock caused by the evolving bubbles. Moreover, the overpotential of NiMo/NF sharply increased when the current density reached 6000 mA cm^{-2}, due to the peeling of the catalyst structure from the substrate at high current densities (Figure S21, Supporting Infor-

mation). In contrast, NiMo/Int/NF retained its morphology after multiple current tests. In durability measurements, the cathode potential of NiMo/Int/NF was maintained for 5000 h (Figure 3d). However, NiMo/NF and Pt/C showed a significant decrease in activity after 1000 h of chronopotentiometry. The XPS, XAFS, and SEM results confirmed that the chemical structure and morphology of NiMo/Int/NF remained stable after short-term catalysis (Figures S22–S25 and Tables S1 and S3, Supporting Information). After 5000 h of HER, although the crystallinity was
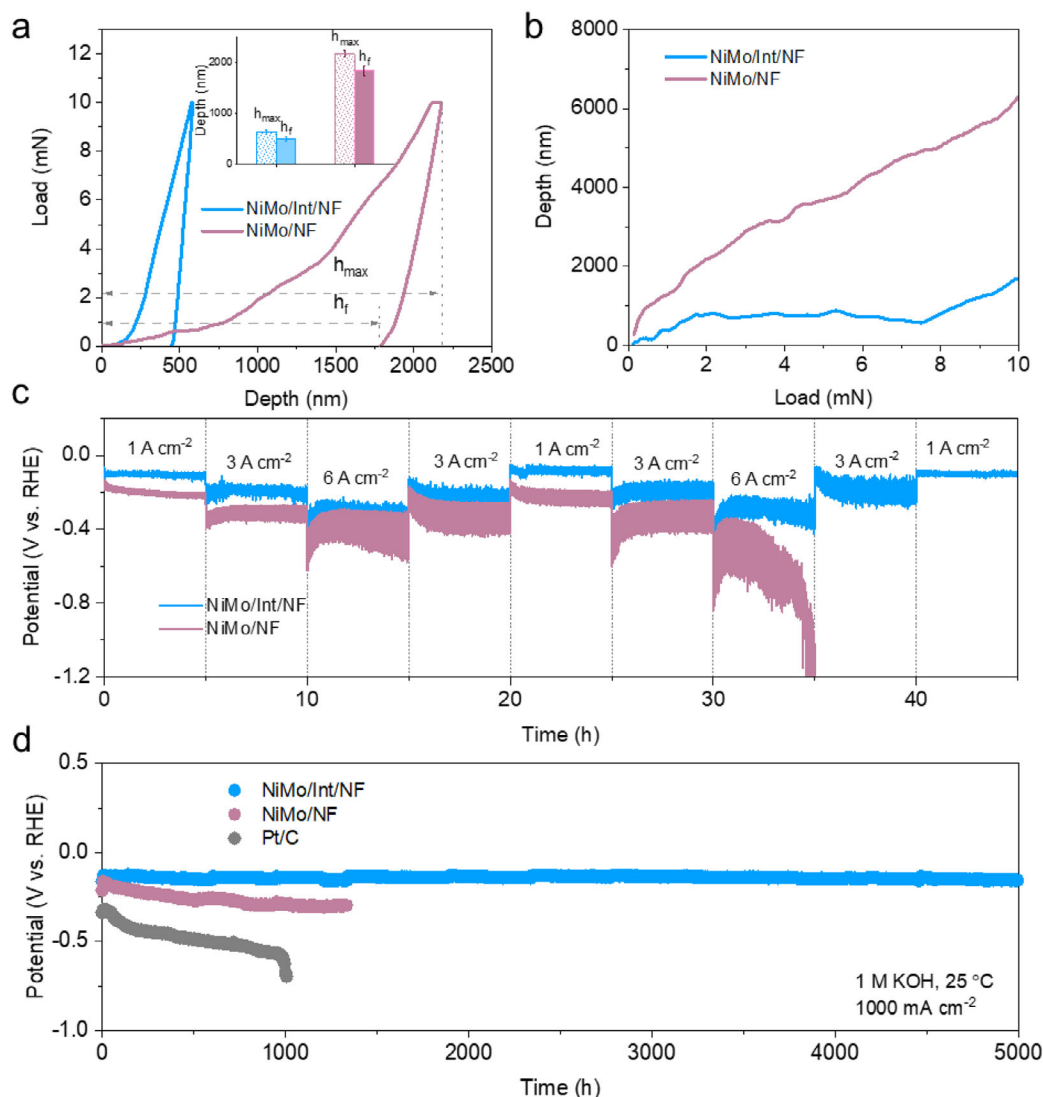
**ADVANCED
SCIENCE NEWS**

www.advancedsciencenews.com

**ADVANCED
MATERIALS**

www.advmat.de

Figure 3. Stability of NiMo/Int/NF. a) Load–displacement curves obtained from nanoindentation measurements for NiMo/Int/NF and NiMo/NF. The inset shows the maximum indentation depth (h_{max}) and the final depth (h_f). b) Load–displacement curves obtained from nanoscratch measurements for NiMo/Int/NF and NiMo/NF. c) Multiple current tests for NiMo/Int/NF and NiMo/NF. d) Stability measurements for NiMo/Int/NF, NiMo/NF, and Pt/C at 1000 mA cm^{-2}.

significantly reduced and a portion of Mo^0 and Mo^{4+} was oxidized to a higher valence state in NiMo/Int/NF (Figure S26, Supporting Information), its morphology and elemental composition remained stable (Figures S27 and S28, Supporting Information). Moreover, the NiMo/Int/NF also showed good HER performance in alkaline seawater (Figure S29, Supporting Information).

The AEM-WE performance was measured in 1 м KOH using NiMo/Int/NF, NiMo/NF, and Pt/C as cathodes. A NiFe catalyst (CAPist-L1)[2c] was used as the anode, and a terphenyl-based poly(aryl piperidinium) polymer (PAP-TP-85) was used as the anion exchange membrane (**Figure** 4a). As shown in Figure 4b, the NiMo/Int/NF-catalyzed noble metal-free AEM-WE device achieves a lower cell voltage (1.78 V) at 1000 mA cm^{-2} and 25 °C, compared to the NiMo/NF-catalyzed electrolyzer (1.89 V) and the Pt/C-catalyzed electrolyzer (1.94 V). Moreover, the cell voltage of CAPist-L1//NiMo/Int/NF is stable at≈1.8 V (1000 mA cm^{-2}) for

3000 h, with a small degradation rate of 22.8 µV h^{-1} (Figure 4c). In contrast, the voltage of the NiMo/NF//CAPist-L1 electrolyzer remains at ≈1.95 V for only ≈200 h and continuously increases to over 2.1 V within 600 h. As shown in Figure 4d and Table S4 (Supporting Information), the NiMo/Int/NF-based noble metal-free electrolyzer outperforms most reported noble metal-free AEM-WE systems.

3. Conclusion

An interlayer-anchored heterostructured electrocatalyst (NiMo/Int/NF) was synthesized using a simple, reproducible, and cost-effective corrosion method, which can be easily scaled up on nickel foil substrates. In 1 м KOH, NiMo/Int/NF showed a low overpotential of 80.2 ± 3.53 mV and a long-term stability for 5000 h at 1000 mA cm^{-2}. Nanoindentation and nanoscratch
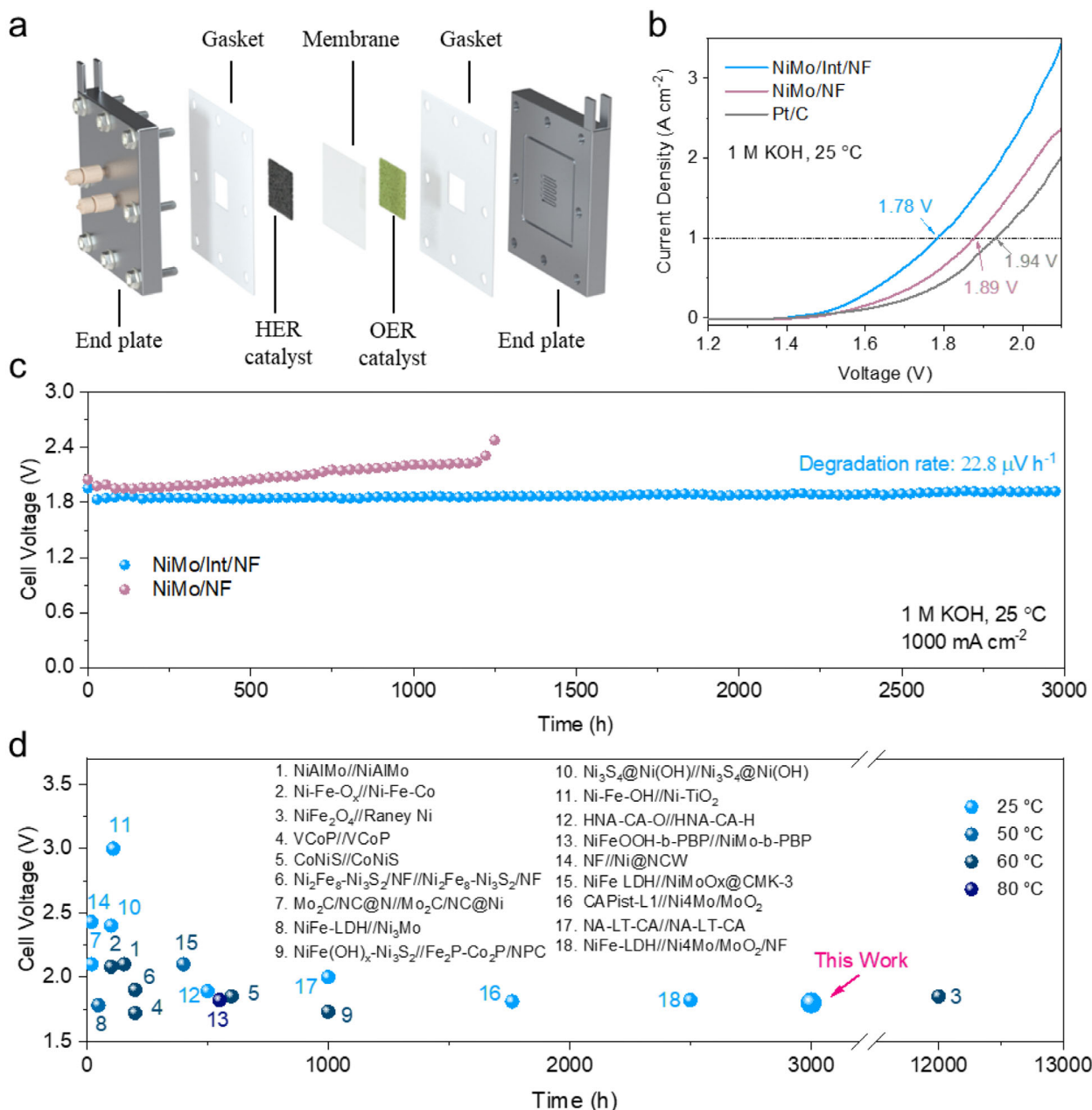
Figure 4. Electrochemical performance of AEM-WE device. a) Schematic of the AEM-WE device. b) Polarization curves of CAPist-L1//NiMo/Int/NF, CAPist-L1//NiMo/NF, and CAPist-L1//Pt/C. c) Stability measurements at 1000 mA cm^{-2}. d) Comparison of the stability time and cell voltage at 1000 mA cm^{-2} of CAPist-L1//NiMo/Int/NF and other recently reported noble metal-free AEM-WE devices. The corresponding references are listed in Table S4 (Supporting Information).

measurements suggested the high mechanical stability of NiMo/Int/NF. Various characterizations confirmed that the heterostructure benefited the fast Volmer step (RDS) and that the interlayer contributed to the high mechanical stability of the catalytic layer. The NiMo/Int/NF-based noble metal-free AEM-WE device achieved high activity and good stability for 3000 h at 1000 mA cm^{-2} with a voltage decrease rate of 22.8 µV h^{-1}. This study provides insights into the design of efficient and robust AEM–WE HER catalysts for industrial hydrogen generation.

Supporting Information

Supporting Information is available from the Wiley Online Library or from the author.

Acknowledgements

[1] a) D. Li, E. J. Park, W. Zhu, Q. Shi, Y. Zhou, H. Tian, Y. Lin, A. Serov, B. Zulevi, E. D. Baca, C. Fujimoto, H. T. Chung, Y. S. Kim, *Nat. Energy* **2020**, *5*, 378; b) N. Wang, S. Song, W. Wu, Z. Deng, C. Tang, *Adv. Energy Mater.* **2024**, *14*, 2303451; c) L. Chong, G. Gao, J. Wen, H. Li, H. Xu, Z. Green, J. D. Sugar, A. J. Kropf, W. Xu, X.-M. Lin, H. Xu, L.-W. Wang, D.-J. Liu, *Science* **2023**, *380*, 609; d) X. W. Lv, W. W. Tian, Z. Y. Yuan, *Electroch. Energy Rev.* **2023**, *6*, 23.

[2] a) D. Henkensmeier, W.-C. Cho, P. Jannasch, J. Stojadinovic, Q. Li, D. Aili, J. O. Jensen, *Chem. Rev.* **2024**, *124*, 6393; b) L. Wan, Z. Xu, Q. Xu, M. Pang, D. Lin, J. Liu, B. Wang, *Energy Environ. Sci.* **2023**, *16*, 1384; c) Z. H. Li, G. X. Lin, L. Q. Wang, H. Lee, J. Du, T. Tang, G. H. Ding, R. Ren, W. L. Li, X. Cao, S. W. Ding, W. T. Ye, W. X. Yang, L. C. Sun, *Nat. Catal.* **2024**, *7*, 944; d) Y. Zheng, W. Ma, A. Serban, A. Allushi, X. Hu, *Angew. Chem., Int. Ed.* **2024**, *64*, 202413698.

[3] a) M. Jin, X. Zhang, S. Niu, Q. Wang, R. Huang, R. Ling, J. Huang, R. Shi, A. Amini, C. Cheng, *ACS Nano* **2022**, *16*, 11577; b) J. Kim, S.-M. Jung, N. Lee, K.-S. Kim, Y.-T. Kim, J. K. Kim, *Adv. Mater.* **2023**, *35*, 2305844; c) J. Zhang, T. Wang, P. Liu, Z. Liao, S. Liu, X. Zhuang, M. Chen, E. Zschech, X. Feng, *Nat. Commun.* **2017**, *8*, 15437; d) M. J. Wu, F. Dong, Y. K. Yang, X. Cui, X. Q. Liu, Y. H. Zhu, D. S. Li, S. Omanovic, S. H. Sun, G. X. Zhang, *Electrochem. Energy Rev.* **2024**, *7*, 10; e) C. Hu, Y. Hu, B. Zhang, H. Zhang, X. Bao, J. Zhang, P. Yuan, *Electrochem. Energy Rev.* **2024**, *7*, 19.

[4] a) H. Liu, R. Xie, Y. Luo, Z. Cui, Q. Yu, Z. Gao, Z. Zhang, F. Yang, X. Kang, S. Ge, S. Li, X. Gao, G. Chai, L. Liu, B. Liu, *Nat. Commun.* **2022**, *13*, 6382; b) Q. Zhang, W. Xiao, W. H. Guo, Y. X. Yang, J. L. Lei, H. Q. Luo, N. B. Li, *Adv. Funct. Mater.* **2021**, *31*, 2102117.

[5] a) A. Bashkatov, S. Park, Ç. Demirkır, J. A. Wood, M. T. M. Koper, D. Lohse, D. Krug, *J. Am. Chem. Soc.* **2024**, *146*, 10177; b) A. Angulo, P. van der Linde, H. Gardeniers, M. Modestino, D. F. Rivas, *Joule* **2020**, *4*, 555; c) S. Park, L. Liu, Ç. Demirkır, O. van der Heijden, D. Lohse, D. Krug, M. T. M. Koper, *Nat. Chem.* **2023**, *15*, 1532; d) M. A. Qadeer, X. Zhang, M. A. Farid, M. Tanveer, Y. Yan, S. Du, Z.-F. Huang, M. Tahir, J.-J. Zou, *J. Power Sources.* **2024**, *613*, 234856.

[6] a) C. Zhang, Z. Xu, N. Han, Y. Tian, T. Kallio, C. Yu, L. Jiang, *Sci. Adv.* **2023**, *9*, add6978; b) X. Xu, G. Fu, Y. Wang, Q. Cao, Y. Xun, C. Li, C. Guan, W. Huang, *Nano Lett.* **2023**, *23*, 629.

[7] a) X. Shi, X. Zheng, H. Wang, H. Zhang, M. Qin, B. Lin, M. Qi, S. Mao, H. Ning, R. Yang, L. Xi, Y. Wang, *Adv. Funct. Mater.* **2023**, *33*, 2307109; b) F.-C. Pan, J. Jia, F. Gong, Y. Liu, S. Liu, S. C. Jun, D. Lin, Y. Guo, Y. Yamauchi, Y. Huo, *ACS Nano* **2024**, *18*, 6202; c) Y. Chen, Y. Liu, W. Zhai, H. Liu, T. Sakthivel, S. Guo, Z. Dai, *Adv. Energy Mater.* **2024**, *14*, 2400059; d) W. Liu, X. Ding, J. Cheng, J. Jing, T. Li, X. Huang, P. Xie, X. Lin, H. Ding, Y. Kuang, D. Zhou, X. Sun, *Angew. Chem., Int. Ed.* **2024**, *63*, 202406082; e) H. S. Hu, X. L. Wang, Z. R. Zhang, J. H. Liu, X. H. Yan, X. L. Wang, J. C. Wang, J. P. Attfield, M. H. Yang, *Adv. Mater.* **2025**, *37*, 2415421; f) F. Gong, Z. Chen, C. Chang, M. Song, Y. Zhao, H. Li, L. Gong, Y. Zhang, J. Zhang, Y. Zhang, S. Wei, J. Liu, *Adv. Mater.* **2025**, *37*, 2415269; g) Y. Zheng, S. Xiao, Z. Xing, H. Wu, T. Ma, Z. Zeng, Y. Liao, S. Li, C. Cheng, C. Zhao, *Nano Energy* **2024**, *127*, 109769; h) J. Fu, G. Yang, Y. Jiao, C. Tian, H. Yan, H. Fu, *Nano Energy* **2024**, *127*, 109727; i) H. Shi, T.-Y. Dai, X.-Y. Sun, Z.-L. Zhou, S.-P. Zeng, T.-H. Wang, G.-F. Han, Z. Wen, Q.-R. Fang, X.-Y. Lang, Q. Jiang, *Adv. Mater.* **2024**, *36*, 2406711.

[8] a) S. Liu, Z. Zhang, K. Dastafkan, Y. Shen, C. Zhao, M. Wang, *Nat. Commun.* **2025**, *16*, 773; b) S. H. Park, D. T. To, N. V. Myung, *Appl. Catal., A* **2023**, *651*, 119013; c) L. Hou, C. Li, H. Jang, M. G. Kim, J.-Z. Jiang, J. Cho, S. Liu, X. Liu, *Adv. Mater.* **2024**, *36*, 2410039; d) A. Nairan, P. Zou, C. Liang, J. Liu, D. Wu, P. Liu, C. Yang, *Adv. Funct. Mater.* **2019**, *29*, 1903747.

[9] a) C. Chen, H. Jin, P. Wang, X. Sun, M. Jaroniec, Y. Zheng, S.-Z. Qiao, *Chem. Soc. Rev.* **2024**, *53*, 2022; b) J. Fan, Z. Feng, Y. Mu, X. Ge, D. Wang, L. Zhang, X. Zhao, W. Zhang, D. J. Singh, J. Ma, L. Zheng, X. Cui, *J. Am. Chem. Soc.* **2023**, *145*, 5710.

[10] a) M. Li, P. Xie, L. Yu, L. Luo, X. Sun, *ACS Nano* **2023**, *17*, 23299; b) R. Iwata, L. Zhang, K. L. Wilke, S. Gong, M. He, B. M. Gallant, E. N. Wang, *Joule* **2021**, *5*, 887.

[11] T. Shinagawa, A. T. Garcia-Esparza, K. Takanabe, *Sci. Rep.* **2015**, *5*, 13801.

[12] a) J. Kibsgaard, T. F. Jaramillo, F. Besenbacher, *Nat. Chem.* **2014**, *6*, 248; b) I. M. Kodintsev, S. Trasatti, *Electrochim. Acta* **1994**, *39*, 1803.

[13] a) Z. Zhang, L. Melo, R. P. Jansonius, F. Habibzadeh, E. R. Grant, C. P. Berlinguette, *ACS Energy Lett.* **2020**, *5*, 3101; b) W. W. Rudolph, G. Irmer, E. Königsberger, *Dalton Trans.* **2008**, *7*, 900.

[14] X. Wang, C. Xu, M. Jaroniec, Y. Zheng, S.-Z. Qiao, *Nat. Commun.* **2019**, *10*, 4876.

[15] a) Y. Yokoyama, K. Miyazaki, Y. Miyahara, T. Fukutsuka, T. Abe, *ChemElectroChem* **2019**, *6*, 4750; b) Y. Yokoyama, K. Miyazaki, Y. Kondo, Y. Miyahara, T. Fukutsuka, T. Abe, *Chem. Lett.* **2020**, *49*, 195.

[16] a) J. Barber, S. Morin, B. E. Conway, *J. Electroanal. Chem.* **1998**, *446*, 125; b) K. Ji, M. Xu, S.-M. Xu, Y. Wang, R. Ge, X. Hu, X. Sun, H. Duan, *Angew. Chem., Int. Ed.* **2022**, *61*, 202209849.

[17] G. Lin, Q. Ju, L. Liu, X. Guo, Y. Zhu, Z. Zhang, C. Zhao, Y. Wan, M. Yang, F. Huang, J. Wang, *ACS Nano* **2022**, *16*, 9920.

[18] a) C. Hu, L. Zhang, J. Gong, *Energy Environ. Sci.* **2019**, *12*, 2620; b) E. R. Sauvé, B. Y. Tang, N. K. Razdan, W. L. Toh, S. Weng, Y. Surendranath, *Joule* **2024**, *8*, 728.

[19] J. Yu, K. Hu, Z. Zhang, L. Luo, Y. Liu, D. Zhou, F. Wang, Y. Kuang, H. Xu, H. Li, H. Duan, X. Sun, *Energy Environ. Sci.* **2023**, *16*, 2068.

[20] A. S. Batchellor, S. W. Boettcher, *ACS Catal.* **2015**, *5*, 6680.